Influence mechanism of defects in aluminum alloy friction stir welding on fatigue life

Ting Jiao
Aircraft Strength Research Institute of China, Xi'an 710065, PR China
296513713@qq.com, https://orcid.org/0000-0002-6377-2150

Junling Fan
Aircraft Strength Research Institute of China, Xi'an 710065, PR China
National Key Laboratory of Strength and Structural Integrity, Xi'an 710065, PR China
Fanjunling623@163.com, https://orcid.org/0000-0002-2093-8632

Xinwei Li, Xiangrui Meng
Aircraft Strength Research Institute of China, Xi'an 710065, PR China
1768390804@qq.com, https://orcid.org/0009-0006-7626-5410
15929909078@163.com, https://orcid.org/0009-0000-0746-9635

Yongbin Ma
School of Mechanics and Transportation Engineering, Northwestern Polytechnical University, Xi'an 710072, PR China
mayb@nwpu.edu.cn, https://orcid.org/0000-0002-3770-4824

ABSTRACT. By controlling welding parameters and adjusting process conditions, three typical defects-oxide inclusions, tunnel defects, and lack-of-penetration defects-were intentionally introduced during the friction stir welding (FSW) of aluminum alloys. A comparative analysis of fatigue *S-N* curves between sound joints and joints with the three types of defects was conducted to systematically evaluate the impact of different defect types on the fatigue performance of welded joints. The results demonstrated that all three defects significantly reduce the fatigue life of the joints, with lack-of-penetration defects having the most pronounced effect, followed by tunnel defects and oxide inclusions. Fracture surface analysis using SEM, EDS, and Microhardness testing confirmed that defects act as the primary crack initiation sites—the sound joint initiated cracks at the arc-textured surface, whereas cracks in all defective joints originated from the defect regions.

Citation: Jiao, T., Fan, J., Li, X., Meng, X., Ma, Y., Influence mechanism of defects in aluminum alloy friction stir welding on fatigue life, Fracture and Structural Integrity, 77 (2026) 362-385.

Received: 22.04.2026
Accepted: 29.05.2026
Published: 05.06.2026
Issue: 07.2026

Building on these fractographic findings, the intrinsic micro-mechanism responsible for the systematic decrease in the S-N curve slope m —from 7.14 for the sound joint to 2.74 for the LOP defect joint—was elucidated: the geometric sharpness and interfacial bonding state of a defect compress the crack initiation stage, shifting the dominant failure mode from initiation-dominated to propagation-dominated, which in turn manifests as a reduction in m .

KEYWORDS. Friction Stir Welding (FSW), Oxide inclusion defects, Tunnel defects, Lack of Penetration Defects (LOP), S-N curve slope, Fatigue failure mechanism.

INTRODUCTION

With the increasing demand for lightweight and long-life structures in modern aviation industry, innovations in advanced materials and joining technologies have become critical for breaking through the bottlenecks of traditional structural design. High-strength aluminum alloys, titanium alloys, and carbon fiber-reinforced composites have been widely applied [1], enabling aircraft such as the Boeing 787 and Airbus A350 to achieve weight reductions of over 20%. However, traditional riveting and fusion welding techniques, due to issues such as low joining efficiency and high residual stresses, are gradually becoming limiting factors in the performance enhancement of lightweight structures. Against this backdrop, friction stir welding (FSW), leveraging its solid-state joining advantages, effectively avoids metallurgical defects such as porosity and hot cracking by eliminating the need for base material melting, while significantly reducing residual stresses [2]. This provides a revolutionary solution for the efficient joining of difficult-to-weld aerospace materials, such as 2XXX and 7XXX series high-strength aluminum alloys [3,4]. Currently, FSW technology has been successfully applied in the manufacturing of aircraft skins, ribs, and fuel tank structures by Boeing and Airbus [5]. The Eclipse E500 commercial aircraft has adopted FSW to replace traditional riveting in its upper and lower wing skins, cabin skins, engine beams, and aft fuselage structures, obtaining FAA certification approval.

However, FSW joints still face performance risks due to defects in complex service environments. Modern fatigue design philosophies have evolved from infinite-life and safe-life concepts to damage tolerance, which explicitly accounts for the presence of initial defects in structural integrity assessments [6]. Despite the obvious process differences, both FSW and AM face a common challenge: the fatigue performance of their products is often controlled by manufacturing defects. In this regard, the advanced quantitative defect-evaluation frameworks developed in AM—including extreme value statistics for defect size distribution, the Murakami equivalent defect area criterion, and probabilistic assessment methods incorporating size effects [6, 7]—offer valuable insights for understanding the detrimental effects of different defect types in FSW joints.

The sensitivity of the welding process window means that improper selection of welding parameters (e.g., insufficient heat input, excessive welding speed) can easily introduce various defects into the weld seam. Nandan et al. [8] pointed out in their FSW review that welding parameters are closely related to material flow behavior, and parameter mismatch can lead to insufficient plastic material flow, thereby inducing defects. Thomas et al. [9] further emphasized in their study of FSW tools and processes that insufficient heat input is a primary cause of lack of penetration (LOP) and tunnel defects. Shi et al. [10] demonstrated in underwater FSW experiments that excessive cooling at a rotational speed of 1200 rpm and a welding speed of 80 mm/min can easily cause cracks in the joint, reducing the ultimate tensile strength by 15.9%. Majeed et al. [11] systematically summarized the formation patterns of various defects, including LOP, tunnel defects, and kissing bonds, through 27 sets of FSW experiments on dissimilar materials with different thicknesses, noting that defect formation is closely related to insufficient material flow and improper thermal cycle control.

Regarding the impact of defects on fatigue performance, existing studies have revealed the detrimental effects of different defect types. Dickerson and Przydatek [12] found that even minor root flaws can reduce the fatigue strength of aluminum alloy FSW joints by more than 30%. Zhou et al. [13] demonstrated that root LOP defects significantly reduce fatigue strength in 2024-T3 aluminum alloy FSW joints, with a clear negative correlation between defect size and fatigue life. Papadopoulos and Pantelakis [14] conducted fatigue experiments on 2198-T8 aluminum alloy FSW joints and found that the fatigue life of specimens with LOP defects dropped to one-tenth that of sound joints at a stress amplitude of 100 MPa, highlighting

the devastating impact of such defects on high-cycle fatigue performance. Rek and Kadlec [15] further indicated that the degree of fatigue life reduction caused by kissing bond defects is closely related to defect size, with larger defects leading to more severe life degradation.

Current research on the fatigue behavior of FSW joints has gradually shifted from qualitative descriptions of the presence or absence of defects to quantitative investigations of the relationship between defect type, size, and service life, as well as the underlying mechanisms. The application of damage tolerance design concepts in welded structures necessitates a systematic understanding of the control mechanisms by which typical defects influence the entire process of crack initiation, propagation, and final failure. This is fundamental for establishing physics-based life prediction models and developing reasonable process tolerance standards. Regarding fatigue testing methods, the work of Sonsino et al. [16] provide important guidance for conducting standardized axial fatigue experiments.

In parallel with these empirical efforts, recent advances in damage tolerance assessment have provided more rigorous theoretical frameworks. For instance, Song et al. [17] proposed a generalized damage tolerance framework that incorporates crack growth behavior and plastic work into a novel failure assessment diagram (FAD), overcoming the physical inconsistency between the static failure boundary and the evolving assessment path in traditional FAD. This framework clearly defines the ligament yielding parameter $L_r = 1$ as the transition criterion for the crack-tip stress state from linear-elastic to elastic-plastic behavior, and establishes a segmented fatigue life prediction model based on this criterion. Such a physically consistent framework offers a solid foundation for understanding how different defect types (e.g., sharp LOP defects vs. rounded oxide inclusions) lead to distinct crack propagation mechanisms.

At the microstructural characterization and failure mechanism level, researchers have conducted extensive work on microstructural evolution around defects, the behavior of secondary phase particles, and crack propagation paths. Sutton et al. [18] revealed through microstructural studies the fine-grained characteristics of the stir zone (SZ) in 2024-T3 aluminum alloy FSW joints, noting that defects often appear in microstructural transition regions. Jata et al. [19] found that grain refinement in the stir zone inhibits fatigue crack initiation, but the presence of defects completely counteracts this beneficial effect. Pujono et al. [20] revealed through fracture morphology and energy-dispersive spectroscopy (EDS) analysis that defect sites are often areas of secondary phase particle aggregation (e.g., Al_2Cu, Al_2CuMg), which easily induce stress concentration and initiate microcracks. Das et al. [21] pointed out in a systematic review that microstructural continuity and metallurgical bonding quality near defects are key factors determining fatigue performance.

Recently, Yang et al. [7] systematically reviewed defect characterization and mechanical property evaluation for additively manufactured mechanical metamaterials, covering defect classification (lack of fusion, gas pores, geometric deviations), multi-scale characterization techniques (micro-CT, in-situ optical monitoring), and statistical models linking defect features to strength and fatigue performance. These methodologies highlight the necessity of quantitatively linking defect morphology, location, and distribution to structural integrity—a concept equally applicable to FSW joints.

At the mechanical behavior level, research has shown that local microstructural changes and hardness gradients induced by defects significantly alter crack propagation paths. Peel et al. [22] demonstrated through studies of residual stress and hardness in AA5083 aluminum alloy FSW joints that the hardness distribution across the weld exhibits a typical “W” shape, with the heat-affected zone (HAZ) and thermo-mechanically affected zone (TMAZ) being the softest regions and most prone to fatigue crack initiation and propagation. Liu et al. [23] further showed that coarsening and dissolution of precipitates in the HAZ are the main reasons for the reduced hardness in this region, with the hardness valley near defects becoming a preferential path for crack propagation. Malopheyev et al. [24] noted in their review of the fatigue performance of aluminum alloy FSW joints that the fatigue life scatter caused by defects is several times larger than that of conventional fusion welds, challenging traditional design methods based on average stress and highlighting the need for probabilistic life assessment based on defect characteristics.

Furthermore, the role of secondary phase particles in fatigue failure mechanisms provides important perspectives for understanding defect effects. McDowell et al. [25] showed through studies on the fatigue behavior of cast aluminum alloys that the distribution state and fragmentation behavior of eutectic silicon particles have a decisive influence on fatigue crack initiation and propagation. Lei et al. [26] further revealed that debonding at the interface between secondary phase particles and the matrix is a primary mechanism of fatigue crack initiation, a mechanism that also applies to crack initiation at oxide inclusions in FSW joints. Lomolino et al. [27] further pointed out in their statistical analysis of fatigue data from various aluminum alloy FSW joints that the fatigue life scatter caused by defects is several times larger than that of conventional fusion welds, challenging traditional design methods based on average stress and highlighting the need for probabilistic life assessment based on defect characteristics.

In summary, although existing research has confirmed the negative impact of defects on the fatigue performance of FSW joints, a systematic comparative study on the “ranking of influence severity” and the underlying "coupling mechanisms" of different defect types (such as oxide inclusions, tunnel defects, and LOP defects) within the same material system is still

lacking. In particular, how the disruption of microstructural continuity and the degradation of metallurgical bonding quality caused by defects jointly determine the degree of fatigue life reduction through their effects on crack initiation and propagation paths, and how such microscopic features are ultimately reflected in macroscopic fatigue parameters still require further elucidation of the underlying physical essence.

This study focuses on AA2024-T3 aluminum alloy FSW joints, systematically introducing three typical defects-oxide inclusions, tunnel defects, and LOP defects-through process parameter control. By integrating fatigue life experiments, S-N curve analysis, and detailed fractographic characterization using SEM and EDS, the influence of each defect type on fatigue performance is comparatively evaluated, and a quantitative severity ranking is established. Furthermore, based on the fractographic evidence, the intrinsic micro-mechanism by which defects reduce the S-N curve slope m is elucidated. The results will provide theoretical support for FSW process optimization, defect tolerance design, and life prediction models, and will have significant engineering value for promoting the large-scale application of this technology in high-reliability aviation structures.

MATERIALS AND EXPERIMENTAL METHODS

To conduct simulation experiments on the friction stir welding of aircraft skin structures, AA2024-T3 aluminum alloy sheets with a thickness of 2 mm were selected as the experimental material. The sheets were subjected to solution treatment followed by natural aging strengthening. The specific chemical composition is shown in Tab. 1, and the room temperature static tensile properties are listed in Tab. 2 [20].

Cu	Mg	Mn	Si	Fe	Zn	Ti	Cr	Al
4.9	1.2	1.2	0.5	0.5	0.25	0.15	0.1	Bal.

Table 1: Chemical composition of AA2024-T3 aluminum alloy sheets (wt%).

Yield Strength / MPa	Tensile Strength / MPa	Elongation / %	Hardness / HV
345	465	15.6	73

Table 2: Static tensile properties of AA2024-T3 aluminum alloy sheets (rolling direction).

FSW experiments were conducted on a FSW-DLM-158A equipment. The welding tool was made of H13 steel with a double-ring shoulder and a right-handed conical threaded pin. The shoulder diameter was 10 mm, and the pin root diameter was 2 mm.

To prepare high-quality sound joints, an optimization of the FSW process parameters for 2 mm thick non-clad AA2024-T3 aluminum alloy sheets was carried out. Based on the analysis of material mechanical properties and process compatibility, the pin length was fixed at 1.81 mm and the welding pressure at 2.8 kN. A L9 orthogonal experiment was then designed, with welding speed (100/200/300 mm/min) and rotational speed (1000/1200/1400 rpm) as variables, aiming to maximize tensile strength. The experimental results showed that when the welding speed was 200 mm/min and the rotational speed was 1000 rpm, the joint tensile strength reached 431 MPa (92.7% of the base material). This parameter combination was therefore determined as the optimal process (see Fig. 1).

This study aims to systematically investigate the influence of defects on fatigue performance. The selection of defect types considered two aspects: the geometric type of the defect (dispersed, linear, and volumetric) and its detectability by non-destructive testing, with the core being the minimum detectable size. Ultimately, oxide inclusions, tunnel defects, and LOP defects were selected as typical representatives. The sizes of tunnel and LOP defects were controlled within the range of 0.2 mm to 0.5 mm [21]. Based on the optimal parameters for sound joints, defects were introduced by controlling parameters according to their formation mechanisms, as follows.

Oxide inclusion defects were introduced by material substitution, using clad AA2024-T3 aluminum alloy with the same welding parameters as for the sound joint. During welding, the surface aluminum oxide layer was broken and incorporated into the weld, forming discontinuously distributed oxide inclusions accompanied by disturbed metal flow lines (Fig. 2(a)).

Tunnel defects were introduced by increasing the welding speed to 800 mm/min and reducing the welding pressure to 1.7 kN, thereby reducing heat input. This led to insufficient material filling on the advancing side, forming a nearly triangular tunnel defect below the pin action zone, with a maximum size of approximately 0.36 mm (Fig. 2(b)). The tunnel defect had a clear contour, with metal flow lines broken at the boundary with the surrounding dense area.

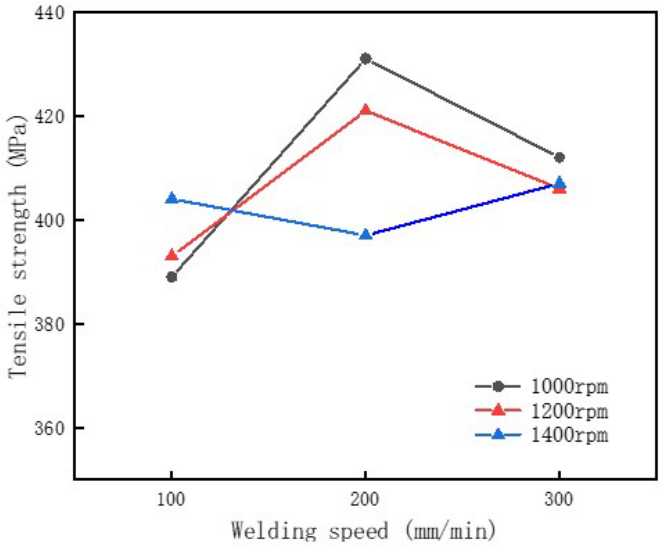

Figure 1: Tensile strength of FSW joints under different welding parameters.

LOP defects were introduced by reducing the pin length from 1.81 mm to 1.53 mm and lowering the welding pressure to 1.8 kN, weakening the thermoplastic flow of material at the weld root and preventing its participation in welding. The LOP defect appeared as an L-shaped crack-like gap, approximately 0.41 mm in size (Fig. 2(c)), with the defect region retaining the original rolled microstructure and showing no obvious plastic deformation.

It should be noted that all fatigue specimens containing the same type of defect (tunnel defect or LOP defect) were sectioned from a single welded plate produced under fixed welding parameters. The defect dimensions reported herein were measured from representative metallographic cross-sections of that plate. Because the welding conditions remained constant during plate fabrication, the defect morphology and size are expected to be reasonably consistent across the specimens. Therefore, individual defect measurement was not performed on every fatigue specimen, and the reported values should be regarded as representative of the defect characteristics under the given welding conditions rather than as statistically characterized quantities.

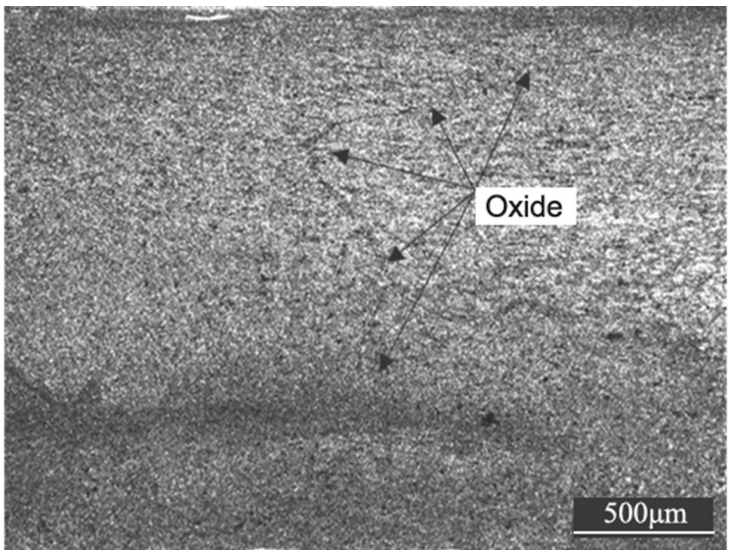

(a) oxide inclusion defects

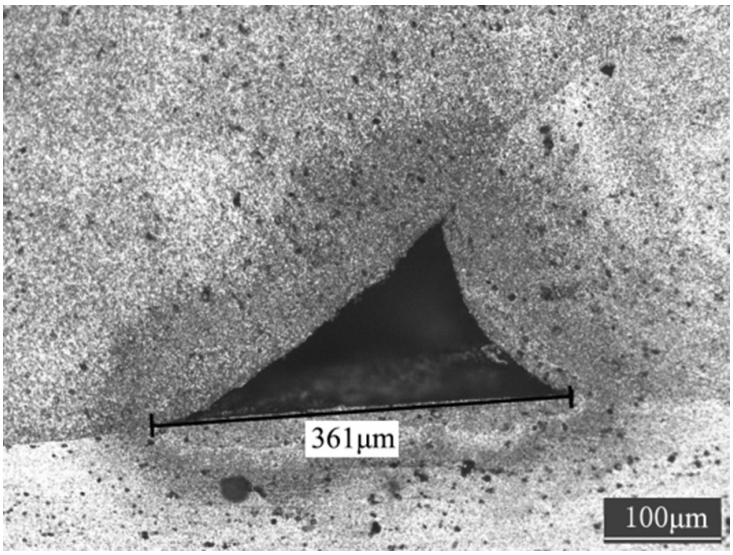

(b) tunnel defects

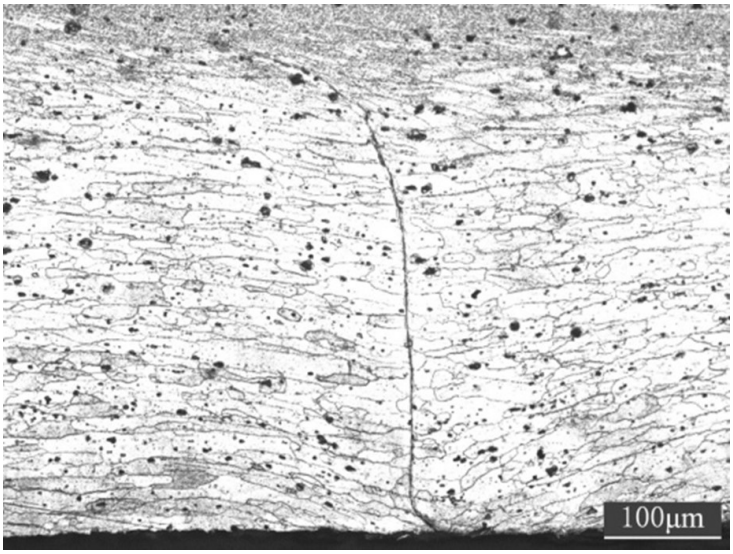

(c) LOP defects

Figure 2: Microstructural characteristics of defects in FSW joints: (a) oxide inclusion defects; (b) tunnel defects; (c) LOP defects.

Fatigue specimens were cut from the welded plates (sound joints and three types of defective joints) according to the shape and dimensions shown in Fig. 3. The specimen length direction was aligned with the material rolling direction.

The weld center was positioned at the axial center of the specimen. To ensure consistent surface conditions, after removing flash from the weld surface, the specimen surfaces were polished along the rolling direction using sandpaper until the surface roughness of the weld surface reached Ra 3.2. The weld root was left in its original state without machining or surface treatment to simulate the possible stress concentration and defect effects at the root in actual structures.

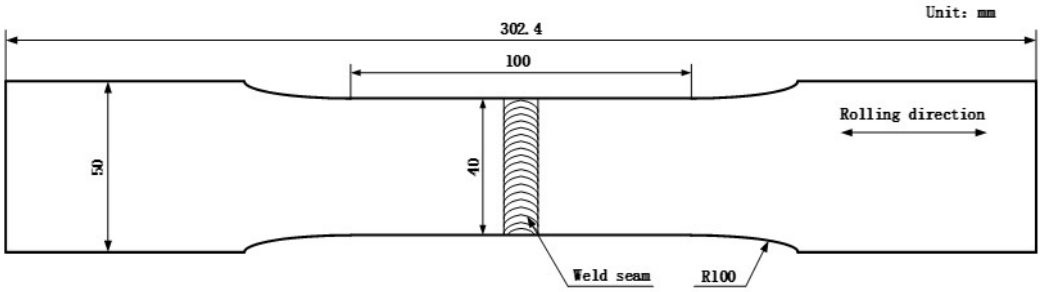

Figure 3: Fatigue test specimen configuration for FSW joints (unit: mm).

According to GB/T 3075-2021 standard of China, fatigue tests were conducted on the FSW sound joint specimens and the three types of typical defective joint specimens (oxide inclusions, tunnel defects, LOP defects) using a low-frequency fatigue testing machine with a rated load of 100 kN. The fatigue loading was constant amplitude sinusoidal wave with a stress ratio of $R = 0.1$ and a loading frequency of 25 Hz. Tests were conducted until specimen fracture, or terminated if the number of cycles reached 2×10^6 without fracture.

To evaluate the hardness distribution characteristics in the weld zones, Vickers hardness tests were conducted at room temperature on the weld cross-sections containing all characteristic zones. Tests were performed along the centerline of the cross-section with a load of 500 g, dwell time of 10 s, and point spacing of 500 μm.

Optical microscopy was used to observe the microstructure and defect morphology of sound joints and the three types of typical defective joints. Fracture surfaces were analyzed using scanning electron microscopy (SEM) combined with energy-dispersive spectroscopy (EDS) to reveal the influence mechanisms of different defect types on crack initiation and propagation behavior.

RESULTS AND DISCUSSION

Given that the stress amplitude ($\Delta\sigma$) under cyclic loading is the governing parameter for the fatigue life of welded joints, the stress amplitude-life ($\Delta\sigma - N$) relationship was used to characterize and study the fatigue performance [16].It should be noted that the FSW process introduces residual stresses into the joint, which may superimpose on the applied load and affect the effective stress ratio at the crack tip. In this study, the welding residual stresses were not measured, and their influence on the effective stress ratio was not considered during fatigue testing.

Fig. 4 shows the fatigue test results for the FSW sound joints and the three types of typical defective joints, plotted on a double logarithmic scale. The results indicate a monotonically decreasing linear relationship between $\lg\Delta\sigma$ and $\lg N$ for all joint types, following a power-law form:

$$N = C(\Delta\sigma)^{-m} \tag{1}$$

where C is a material constant and m is the inverse slope of the $\Delta\sigma - N$ curve. Since fatigue life follows a log-normal distribution, the least squares method was used to fit the experimental data for each group, yielding the linear expression:

$$\lg\Delta\sigma = A - B\lg N \tag{2}$$

where A and B are fitting constants ($B > 0$). The relationship between m and B is:

$$m = \frac{1}{B} \tag{3}$$

Furthermore, the material constants C_i (i=1,…,n) were calculated for each fatigue data point $\Delta\sigma_i$ Their mean value C_m represents the characteristic value at 50% survival probability:

$$C_m = \frac{1}{n}\sum_{i=1}^{n} C_i \tag{4}$$

Finally, the fatigue strength $\Delta\sigma_m$ at 50% survival probability for a target number of cycles N is:

$$\Delta\sigma_m = \left(\frac{C_m}{N}\right)^{1/m} \tag{5}$$

The m values reported in Tab. 3 were obtained by least-squares linear regression of the experimental data for each joint type. To evaluate the statistical scatter of m, the corresponding m_i value for each data point $(\Delta\sigma_i, \mathrm{N}_i)$ was calculated as:

$$m_i = -\frac{\lg C - \lg N_i}{\lg \Delta\sigma} \tag{6}$$

where C is the material constant in Eqn. (1). The standard deviation of m for each group was then determined by [28]:

$$Stdv\ m = \sqrt{\frac{1}{n-1}\sum_{i=1}^{n}(m_m - m_i)^2} \tag{7}$$

where n us the number of valid data point in the group, and m_m is the arithmetic mean of the m_i values. The standard deviations of m for all joint types are reported in Tab. 3. The 95% confidence intervals for each S-N curve are shown as a shaded bands in Fig. 4, reflecting the scatter of the experimental data.

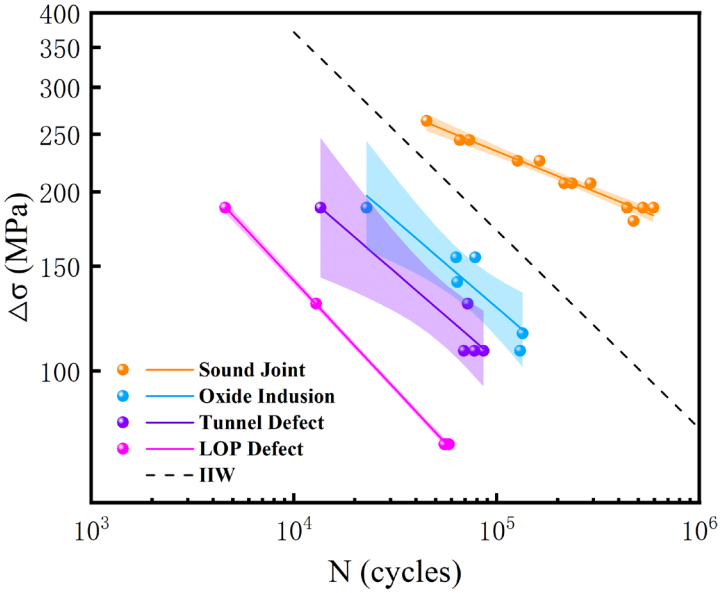

Figure 4: Fatigue S-N curves of FSW joints.

Joint Type	m	C_m	$\Delta\sigma_m$ / MPa		Fatigue strength retention		$Stdv\ m$	r
			2×10^5 cycles	2×10^6 cycles	2×10^5 cycles	2×10^6 cycles		
Sound Joint	7.14	7.96×10^{21}	210.8	152.7	100%	100%	0.0322	0.981
Oxide Inclusion	3.41	1.55×10^{12}	104.3	53.1	49.5%	34.8%	0.0533	0.926
Tunnel Defect	3.39	6.94×10^{11}	85.0	43.1	40.3%	28.2%	0.0521	0.952
LOP Defect	2.74	7.83×10^{9}	47.5	20.5	22.5%	13.4%	0.0045	0.999

Table 3: S-N curve parameters and fatigue strength retention percentages of FSW joints.

To establish a unified quantitative metric for comparing the severity of different defect types, the fatigue strength of the sound joint at each target life is taken as the baseline. For 2×10^5 cycles and 2×10^6 cycles, the fatigue strength retention percentage of each defective joint relative to the sound joint is calculated and listed in Tab. 3. Both cycle levels are used for independent quantitative comparison, eliminating the ambiguity of a single-point evaluation.

Tab. 3 presents the fitted S-N parameters and the fatigue strength of each joint type at 2×10^5 cycles and 2×10^6 cycles. For the sound joint, the fatigue strength is 210.8 MPa at 2×10^5 cycles and 152.7 MPa at 2×10^6 cycles. At 2×10^5 cycles, the retention percentages of the joint with oxide inclusion, tunnel, and LOP defects are 49.5%, 40.3%, and 22.5%, respectively. At 2×10^6 cycles, the retention percentages become 34.8%, 28.2%, and 13.4%, respectively. These quantitative metrics consistently rank the defect severity: LOP defect > tunnel defect > oxide inclusion defect at both life levels, confirming that defect significantly weaken the fatigue performance of the joints.

From the perspective of the S-N curve slope, the sound joint exhibits a m value of 7.14, substantially higher than the typical value of 3.0 for fusion-welded joints. On a double-logarithmic plot, its curve appears relatively flat, indicating a high sensitivity of fatigue life to variations in stress amplitude: a small reduction in $\Delta\sigma$ leads to a pronounced extension of life, making it well-suited for long-life applications. The m values of the three defective joints drop to 3.41, 3.39 and 2.74, respectively, with sensitivity decreasing accordingly. The ability of stress amplitude adjustments to influence fatigue life thus weakens, and the fatigue behavior of these joints approaches that of conventional fusion-welded joints.

For comparison, the IIW-recommended S-N curve for aluminum alloy butt-welded joints (the fatigue strength is 80 MPa at 2×10^6 cycles, slope $m=3$) is included in Fig. 4 as a dashed line [29]. Since the IIW recommendations do not specify a fatigue strength class for the AA2024, the 80 MPa for the 7XXX series (also a high-strength aluminum alloy) is adopted here as the reference. The sound joint lies well above this reference curve across the entire stress range, which is consistent with the superior fatigue performance typically achieved by FSW over fusion welding.

The two quantitative metrics, namely the fatigue strength retention percentage and the S-N curves slope m, provide a quantifiable standard for evaluating the severity of defects in FSW joints from two dimensions: fatigue strength loss and sensitivity to stress amplitude variation.

Furthermore, the location of fatigue fracture along the specimen length also showed differentiated characteristics (the marks in Fig. 5 indicate the fatigue fracture location across the specimen width): sound joints fractured in the base material (parallel section of the specimen) or at the advancing side shoulder edge (approximately 5 mm from the nugget center, see Fig. 5(a)); oxide inclusion defective joints fractured on the advancing side (approximately 1.5 mm from the nugget center, see Fig. 5(b)); tunnel defective joints fractured on the retreating side (approximately 1 mm from the nugget center, see Fig. 5(c)); and LOP defective joints fractured at the nugget center (see Fig. 5(d)). The fatigue fracture locations reflect the dominant role of defects in crack initiation.

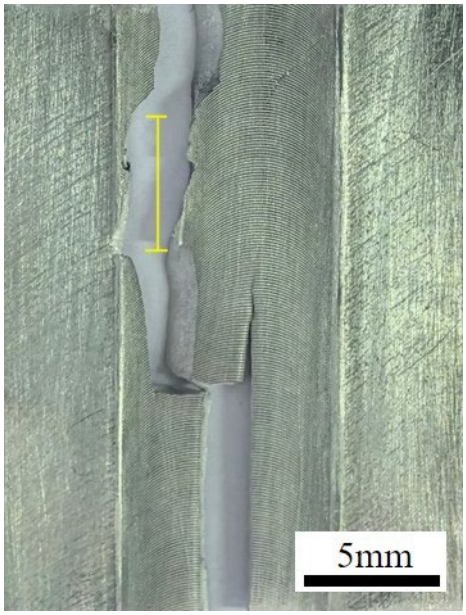

(a) sound joint

(b) joint with oxide inclusion defect

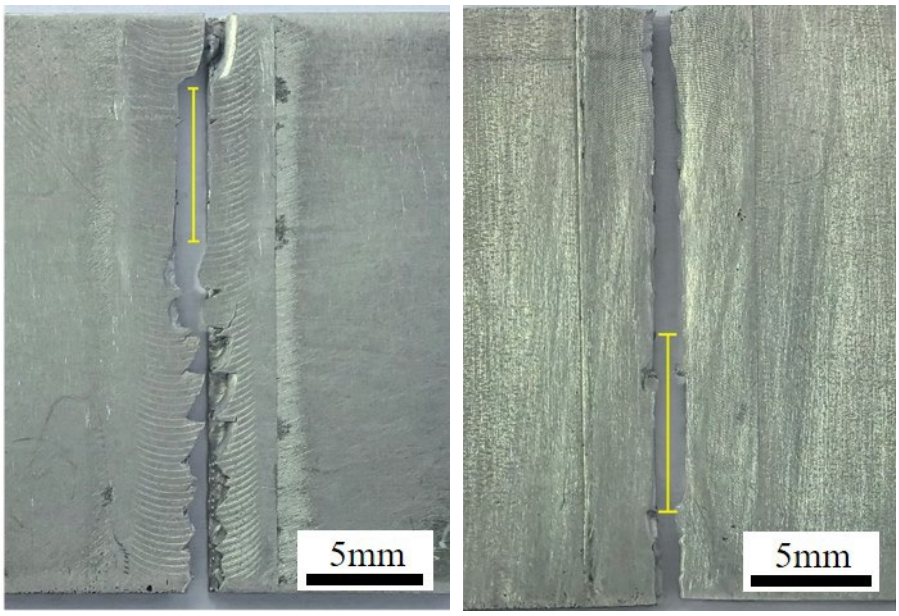

(c) joint with tunnel defect (d) joint with LOP defect

Figure 5: Fatigue fracture location of FSW joints: (a) sound joint; (b) joint with oxide inclusion defect; (c) joint with tunnel defect; (d) joint with LOP defect.

To systematically investigate the influence of defects on fatigue failure in FSW joints, this study combined macroscopic fracture morphology observation with microscopic fracture analysis (SEM, EDS, hardness testing) to reveal the mechanisms of crack initiation, propagation, and fracture for different defective joints. Detailed analyses are presented by defect type.
As shown in Fig. 6, the macroscopic fracture surface of the sound joint shows a single crack initiation site near the arc-striated surface on the advancing side, propagating through the thickness toward the root. The main crack path has a regular arc shape, with uniformly distributed radial striations on the surface, indicating a stable crack propagation process. The fracture surface is smooth and flat, with no obvious brittle fracture areas, reflecting good overall toughness of the joint.

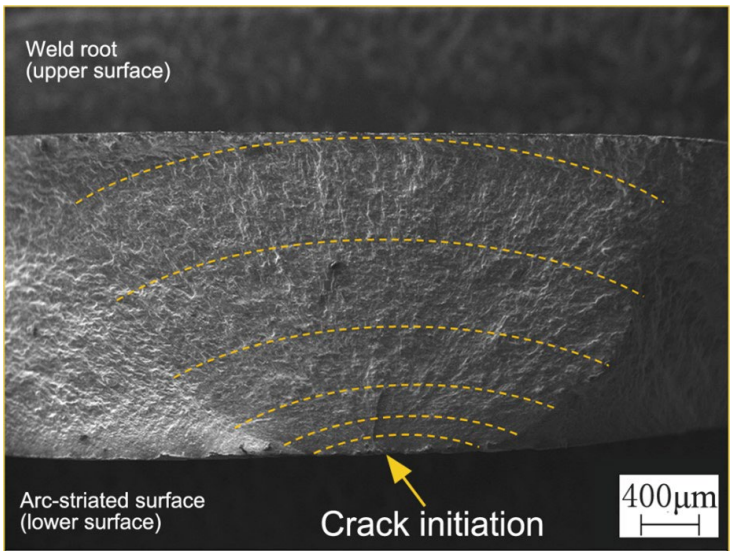

Figure 6: Fatigue fracture morphology of a sound joint observed via low-magnification SEM.

The crack initiation zone of the sound joint (Fig. 7(a)) is smooth and free of fatigue striations, with shallow pits locally formed by the spalling of Al-Cu-Mg compounds (S phase). The propagation zone (Fig. 7(b)) exhibits regular fatigue striations (average spacing 50 nm), accompanied by tearing ridges and secondary cracks, indicating that crack propagation was hindered at grain boundaries and secondary phase boundaries. The final fracture zone (Fig. 7(c)) is dominated by dense

equiaxed dimples (diameter 100–300 nm), with some dimples showing traces of extracted precipitates, suggesting microvoid coalescence as the dominant fracture mechanism.

As shown in Fig. 8, the microhardness distribution across the width of the sound joint exhibits a "W" shape [23]. The stir zone has the highest hardness (HV 150 ± 5), followed by the TMAZ (HV 140 ± 3), while the HAZ reaches its lowest value (HV 130 ± 4), all lower than the base material hardness (HV 160 ± 5). In the TMAZ/HAZ transition region, a hardness gradient as high as 10 HV/mm leads to material softening, thereby increasing the local stress concentration factor. This indicates that the TMAZ/HAZ softened region is the strength-weak link of the joint and the area most prone to fatigue crack initiation.

In terms of microstructure (Fig. 9(a)), the base material exhibits elongated grains with a distinct rolling texture, with an average size of 50–70 μm. In contrast, the stir zone has undergone dynamic recrystallization, forming fine equiaxed grains with low dislocation density (Fig. 9(b)), with an average grain size of only 1–5 μm. This significant grain refinement positively contributes to improving the fatigue performance of the joint.

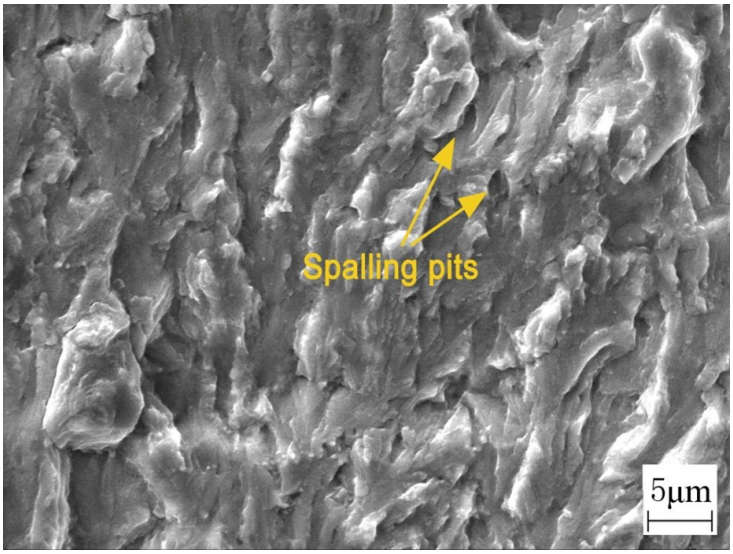

(a) crack initiation zone

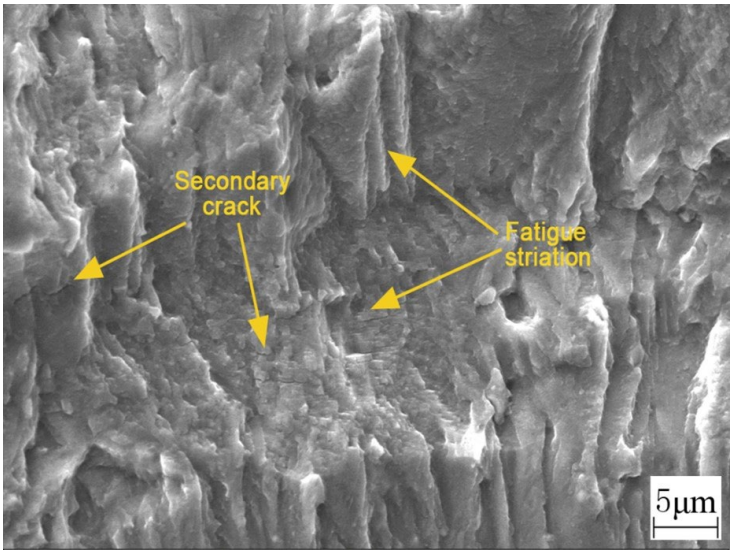

(b) crack propagation zone

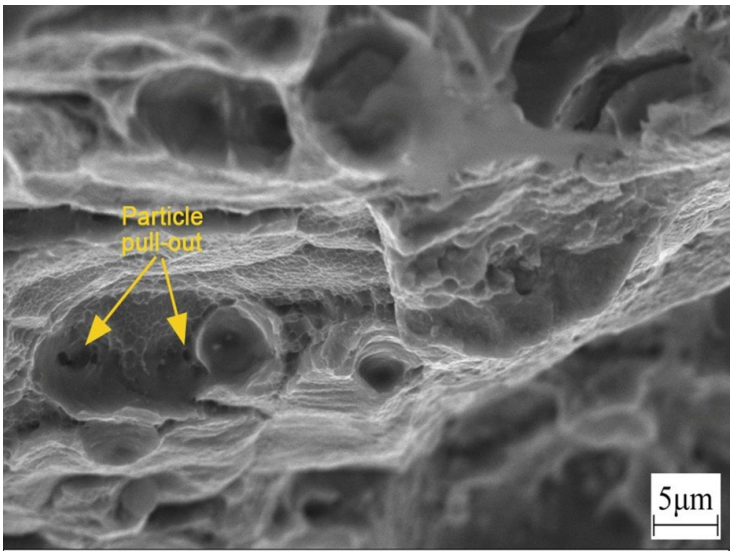

(c) final fracture zone

Figure 7: Fatigue fracture morphology characteristics of a sound joint observed via high-magnification SEM: (a) crack initiation zone; (b) crack propagation zone; (c) final fracture zone.

In summary, the fatigue behavior of the sound joint is essentially the result of the interplay between two competing microstructural mechanisms introduced by the FSW process: the strengthening effect due to grain refinement in the stir zone and the weakening effect due to material softening and stress concentration in the HAZ [24].

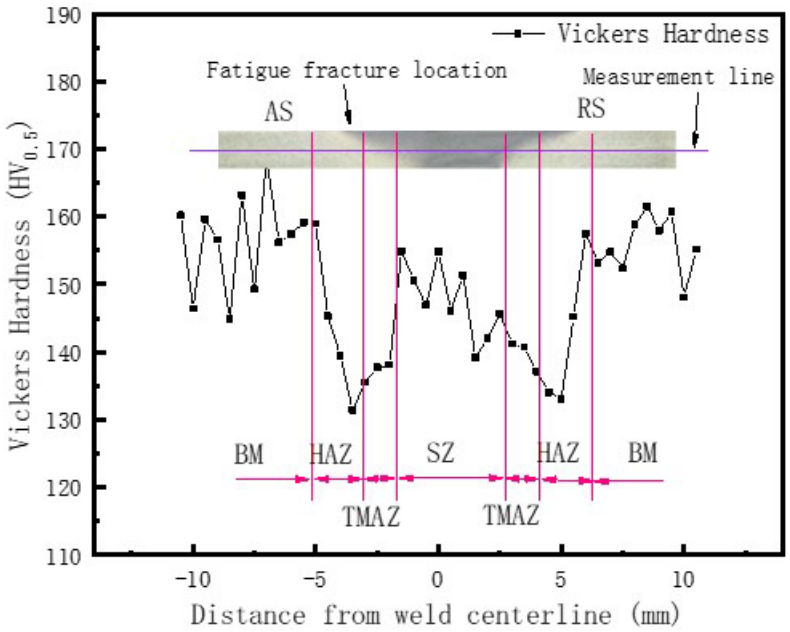

Figure 8: Microhardness distribution in a sound joint.

For the joint with oxide inclusion defects (Fig. 10), the crack initiation sites are concentrated in the weld root area. Cracks rapidly propagate transversely across the joint width. Multiple cracks merge into a main crack during propagation, extending toward the arc-striated surface. The fracture surface has fewer radial striations, which are gently curved, indicating that crack propagation is dominated by the physical barrier effect of the inclusion defects, resulting in less consistent propagation paths.

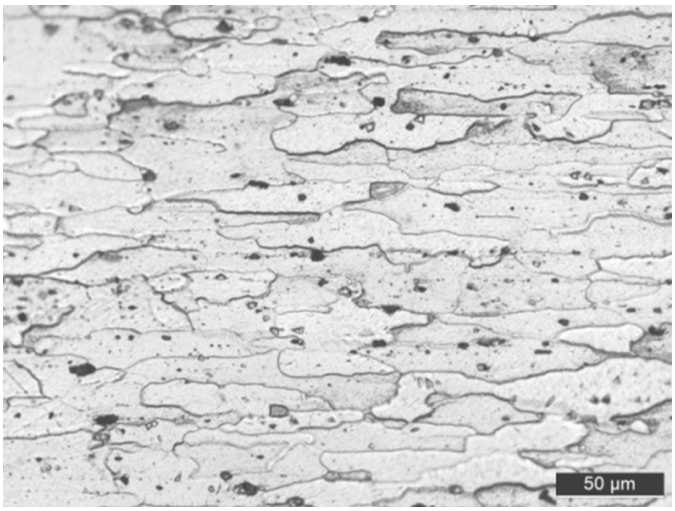

(a) base material

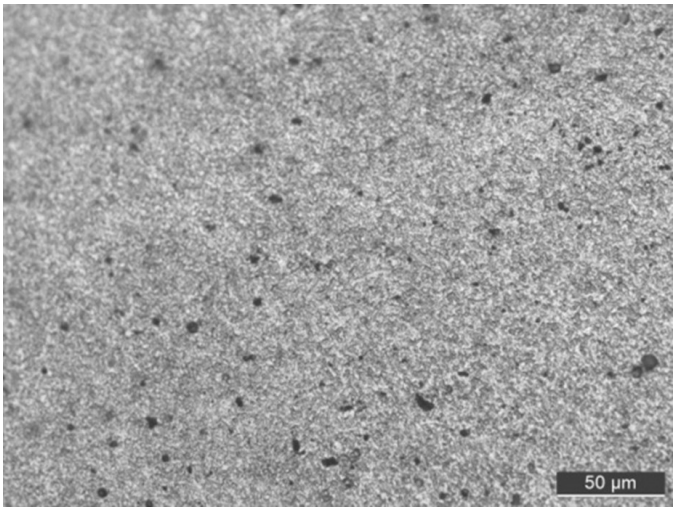

(b) stir zone of sound joint

Figure 9: Microstructural comparison between base material and stir zone of sound joint: (a) base material; (b) stir zone of sound joint.

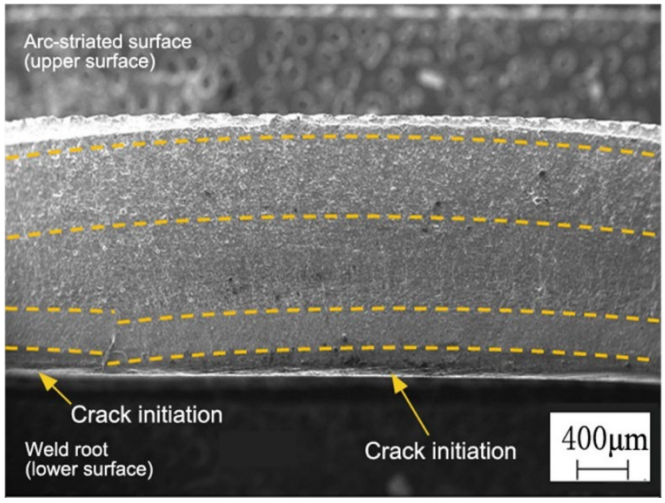

Figure 10: Fatigue fracture morphology of a joint with oxide inclusion defect observed via low-magnification SEM.

The crack initiation zone of the joint with oxide inclusion defects (Fig. 11(a)) is rough, with no obvious fatigue striations. Bright white granular structures are present locally, identified as Al_2O_3 inclusions (EDS analysis shows oxygen content of 7.3 wt%, with local peaks up to 10.9 wt%). The propagation zone (Fig. 11(b)) exhibits a rough fracture surface with multidirectional propagation, featuring inclusion tearing ridges and fragmented surfaces. The final fracture zone (Fig. 11(c)) displays both ductile dimples (diameter 50–200 nm) and quasi-cleavage fracture (some areas appear flat due to crack propagation along the oxide inclusion interface), with some regions showing original dendritic boundaries.

As shown in Fig. 12, oxide inclusions are enriched in the weld root area (average oxygen content 7.3 wt%), while only 1.5 wt% is present in the central region. This uneven distribution leads to the following failure mechanisms:

The bond strength between oxides and the matrix is weak, leading to early fracture or interface debonding. Sharp defects generated by coarse particle fracture or debonding locally amplify the stress, making the local crack stress intensity factor significantly higher than that corresponding to the macroscopic stress, thereby significantly reducing the number of cycles required for crack initiation [25,26].

The random distribution of inclusions along the thickness direction forces cracks to propagate in multiple directions, reducing energy dissipation efficiency. Local crack growth rates were estimated from fatigue striation spacing measurements. Under the same nominal stress amplitude, the striation spacing measured in the oxide inclusion defect joint was approximately 2.5×10^{-7} m/cycle, about four times that obtained at a comparable location in the sound joint.

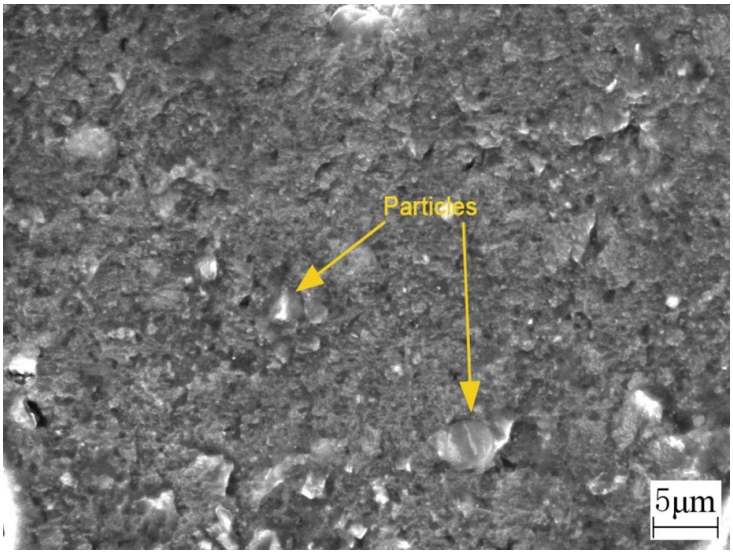

(a) crack initiation zone

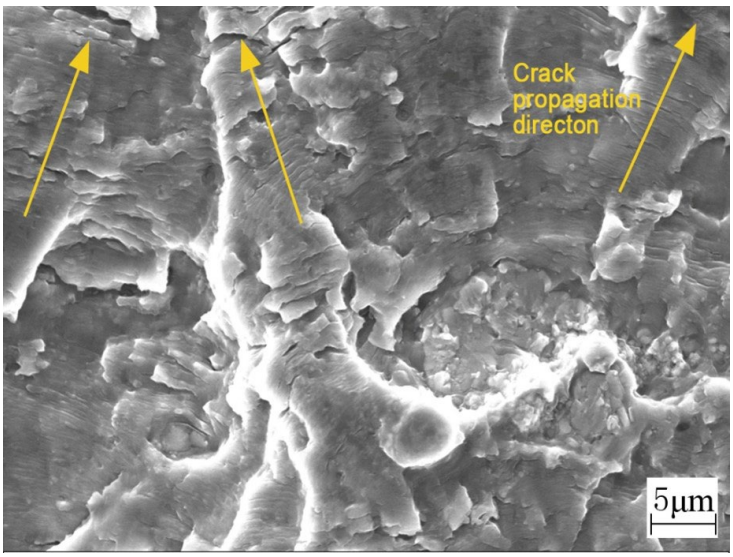

(b) crack propagation zone

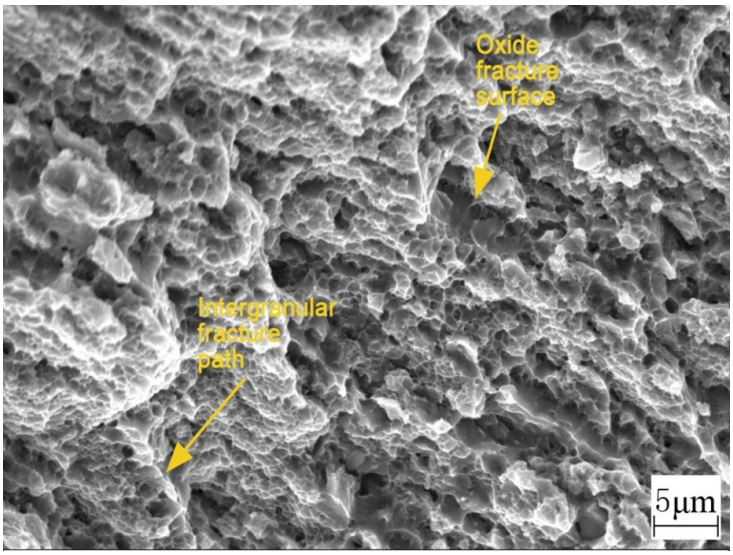

(c) final fracture zone

Figure 11: Fatigue fracture morphology characteristics of a joint with oxide inclusion defect observed via high-magnification SEM: (a) crack initiation zone; (b) crack propagation zone; (c) final fracture zone.

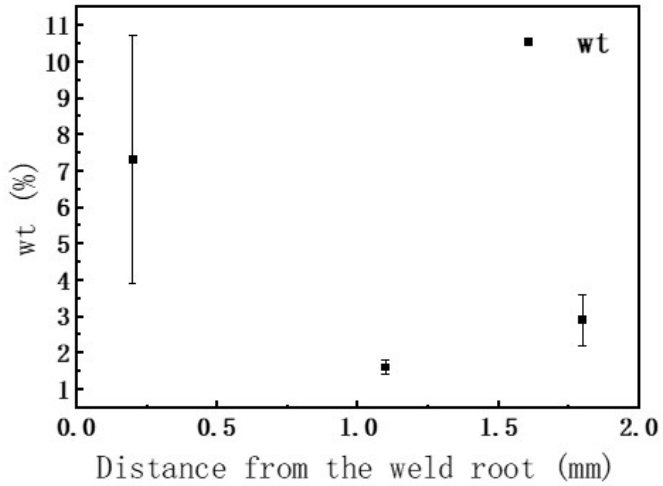

Figure 12: Oxygen mass percentage distribution in the fatigue fracture of a joint with oxide inclusion defect.

As shown in Fig. 13, the macroscopic fracture surface of the joint with tunnel defects exhibits multiple crack initiation sites distributed along the width direction, concentrated at the interface between the root and the tunnel defect. The multiple cracks merge into a main crack farther from the root, indicating significant differences in the initiation times of individual cracks, caused by the considerable variation in the size and morphology of the tunnel defect along the specimen width direction.

From the crack path shown in Fig. 14, it is evident that fatigue failure in the joint with tunnel defect begins at the stress concentration at the edge of the defect (point ∠A). During the subsequent stable propagation stage, the direction perpendicular to the applied load becomes the dominant mechanism, causing the crack path to completely engulf the tunnel defect, making it part of the fracture surface.

The crack initiation zone (Fig. 15(a)) shows a lamellar structure, indicating insufficient local plastic deformation, with local microvoids (diameter 1–3 μm). The propagation zone (Fig. 15(b)) features a rough, undulating fracture surface, suggesting that the internal structure of the material is not tightly bonded or that local microstructural changes have occurred. Fatigue striations and secondary cracks are visible in this region, indicating stable crack propagation under multiple loading cycles. The final fracture zone (Fig. 15(c)) consists of a coarse-grained upper region (grain size 8 μm) and a fine-grained dimple lower region (diameter 100–500 nm), indicating inhomogeneous microstructure due to insufficient heat input at the root.

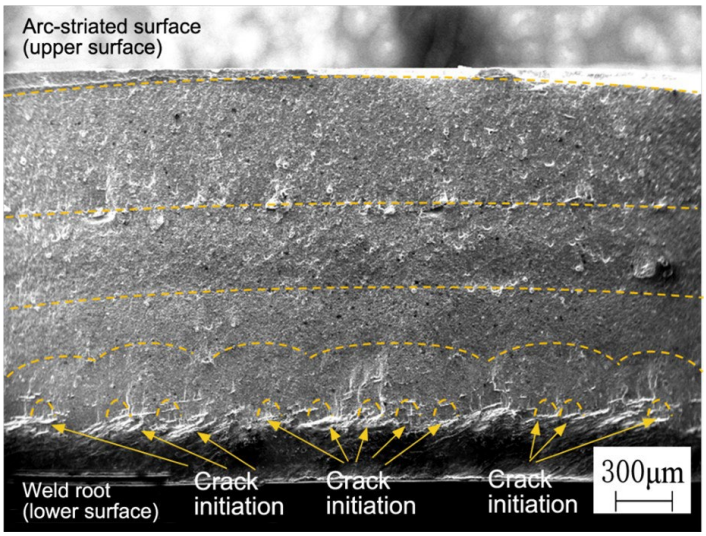

Figure 13: Fatigue fracture morphology of a joint with tunnel defect observed via low-magnification SEM.

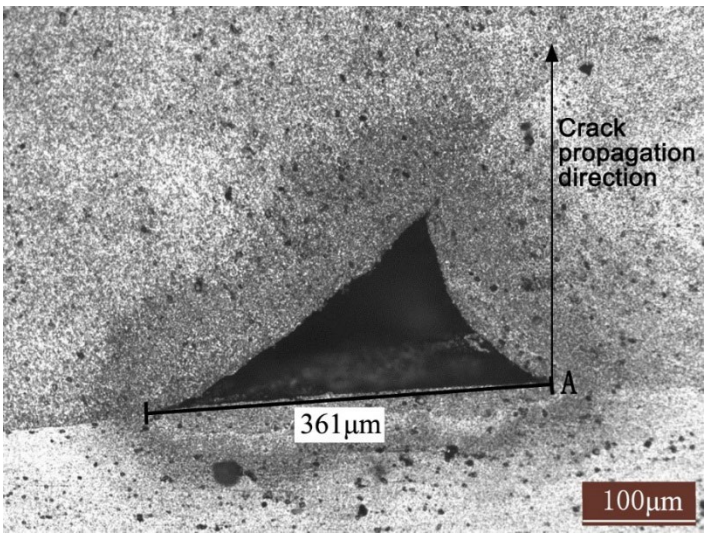

Figure 14: Schematic diagram of crack initiation and propagation path in a joint with tunnel defect.

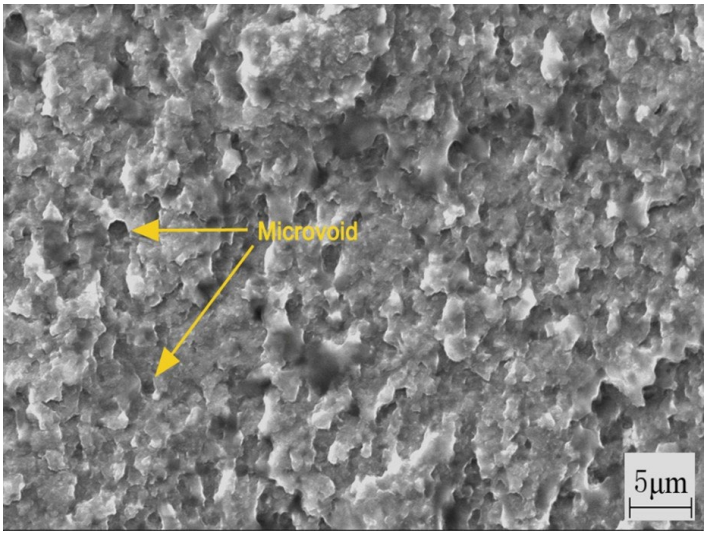

(a) crack initiation zone

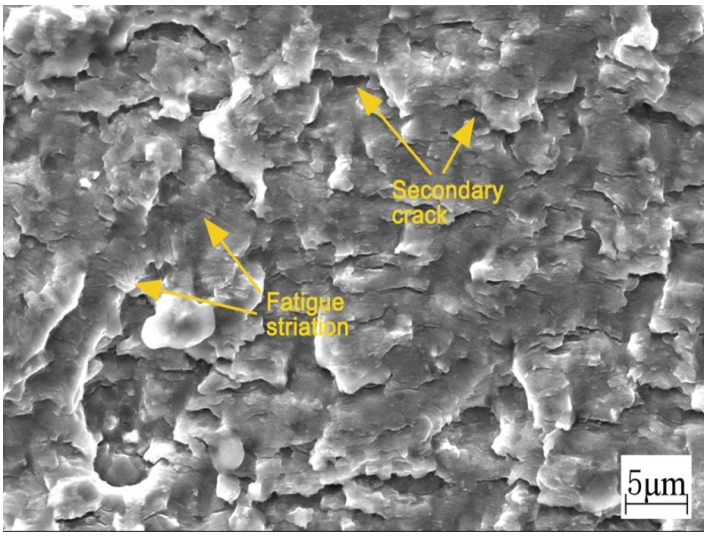

(b) crack propagation zone

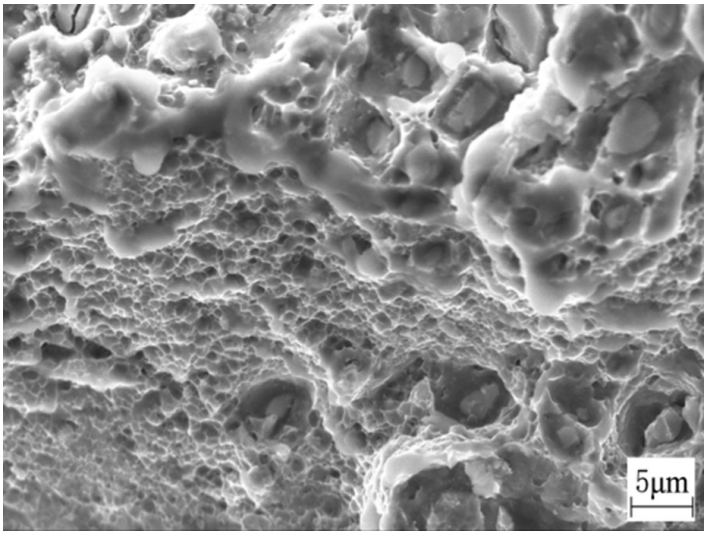

(c) final fracture zone

Figure 15: Fatigue fracture morphology characteristics of a joint with tunnel defect observed via high-magnification SEM: (a) crack initiation zone; (b) crack propagation zone; (c) final fracture zone.

High-magnification SEM observation (Fig. 16) reveals that the fracture surface in the area from point ∠A to the weld root lacks features of plastic or brittle fracture, indicating that no effective metallurgical bond was formed in this region, presenting the characteristic structure of a kissing bond defect. Although the materials appear to be in close contact macroscopically (Fig. 14), the microscopic interface is only connected through mechanical interlocking without atomic-level diffusion bonding (Fig. 16(b)), resulting in near-zero interfacial strength. This means that this region did not participate in effective crack propagation during fatigue crack growth nor bear residual strength, providing no positive contribution to the overall fatigue performance of the joint.

Fatigue failure in the joint with tunnel defect is caused by the superimposed coupling effect of the tunnel defect and the kissing bond defect, reflecting the combined effect of geometric discontinuity and interface weakness. The geometric discontinuity of the tunnel defect leads to a high stress concentration factor, while the kissing bond defect induces stress concentration due to its weak interface bond. The intersection of these two defects becomes a preferential region for crack growth. This composite defect is a key factor for early fatigue crack initiation and rapid propagation, significantly degrading the fatigue performance of the joint.

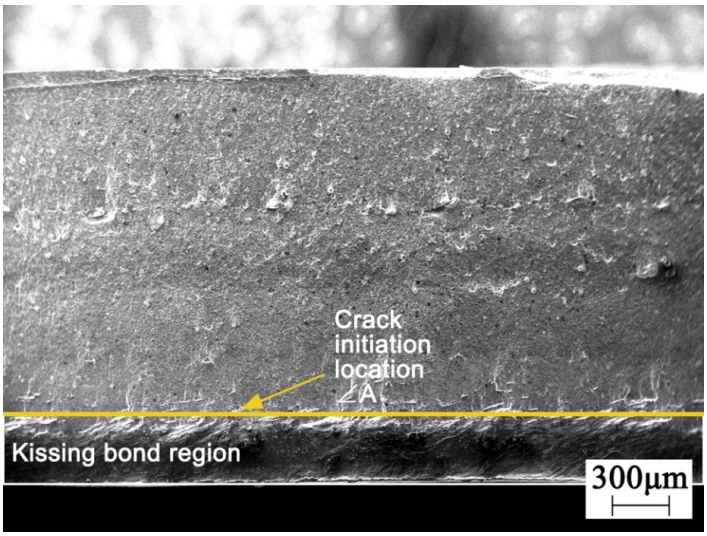

(a) macroscopic morphology of the kissing bond region

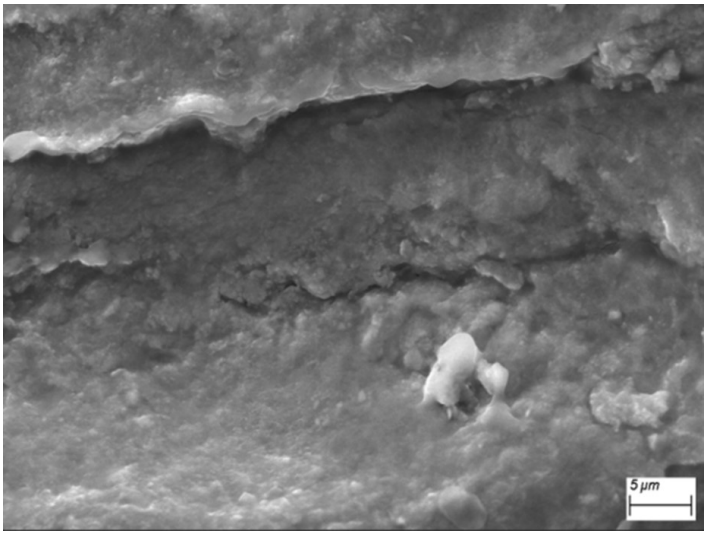

(b) microscopic morphology of the kissing bond region

Figure 16: Morphology characteristics of the kissing bond in a joint with tunnel defect: (a) macroscopic morphology of the kissing bond region; (b) microscopic morphology of the kissing bond region.

As shown in Fig. 17, the macroscopic fracture surface of the joint with LOP defects exhibits multiple crack initiation sites concentrated at the edge of the weld root. The multiple cracks initiate at nearly the same time, forming a main crack rapidly with a short and straight path. The radial striations are dense and directionally consistent.

The crack initiation zone of the joint with LOP defects (Fig. 18(a)) is generally flat, with dense fatigue striations extending in an arc pattern. The striations have uniform width and are evenly distributed, indicating rapid crack initiation under low plasticity conditions. The propagation zone (Fig. 18(b)) exhibits a layered tearing characteristic, with tear step structures visible along the propagation path. Smooth slip planes are visible locally, reflecting the influence of microstructural heterogeneity on the crack propagation path. The final fracture zone (Fig. 18(c)) shows unevenly distributed dimples (size 50–500 nm), with local tearing ridges and shear lips indicating inhomogeneous plastic deformation during the fracture process.

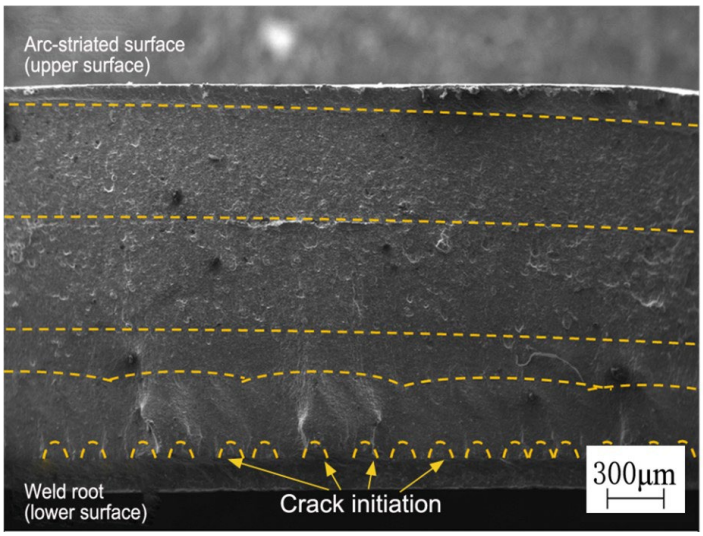

Figure 17: Fatigue fracture morphology of a joint with LOP defect observed via low-magnification SEM.

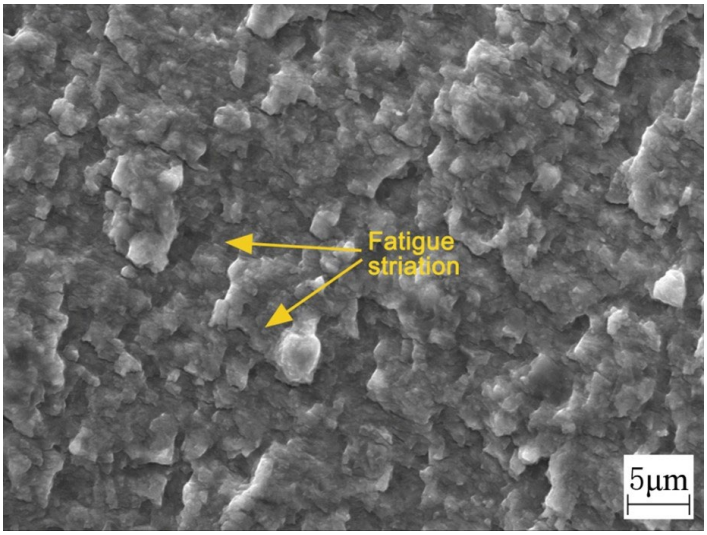

(a) crack initiation zone

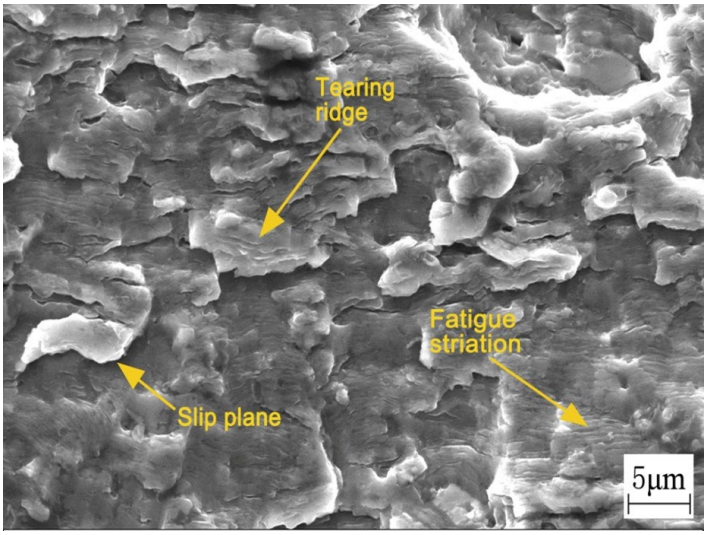

(b) crack propagation zone

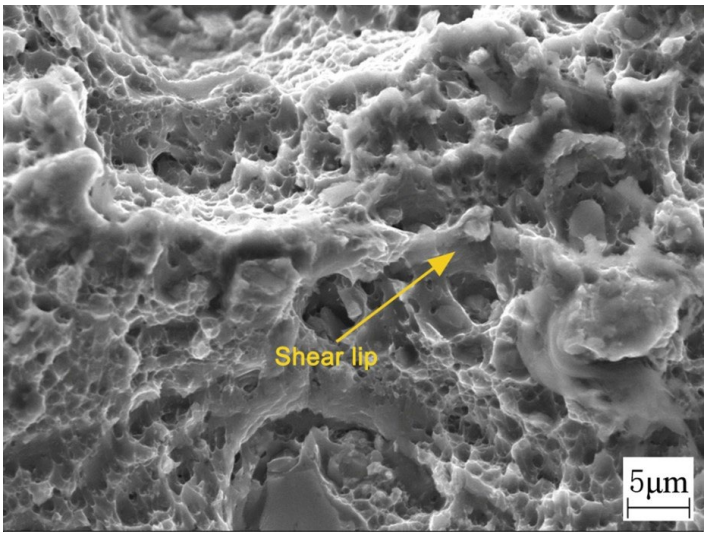

(c) final fracture zone

Figure 18: Fatigue fracture morphology characteristics of a joint with LOP defect observed via high-magnification SEM.

LOP defects are the most dangerous fatigue crack initiation sites in FSW joints. Macroscopically, this defect not only disrupts joint integrity, but its tip also acts as a significant stress concentration point, accelerating fatigue crack initiation. Microscopically, insufficient heat input leads to incomplete dynamic recrystallization, forming a coarse (> 10 μm) and heterogeneous grain structure (see Fig. 19), providing preferential paths for crack initiation and propagation. The dense fatigue striations appearing in the crack initiation zone indicate that cracks initiate rapidly at the defect site almost without relying on plastic accumulation, which is a key microstructural characteristic underlying the significant reduction in joint fatigue life. Therefore, despite its simple morphology, LOP defects pose an extremely high risk of fatigue failure.

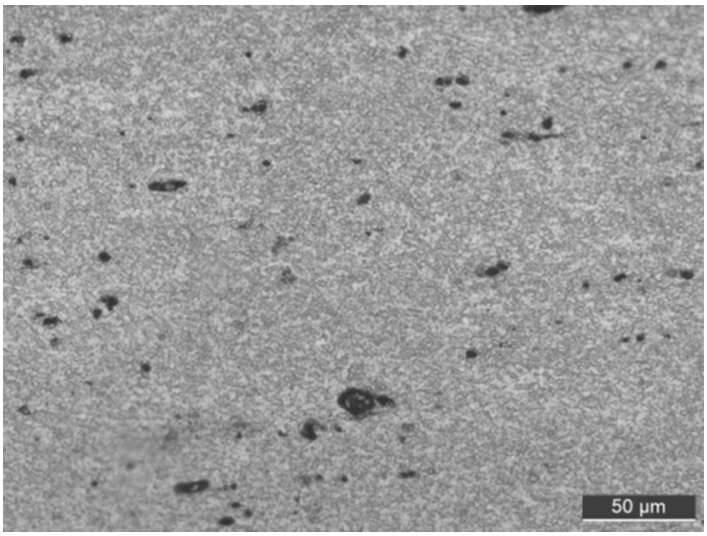

Figure 19: Microstructure of the stir zone in a joint with LOP defect.

The fatigue results reveal a systematic decrease in the S-N curve slope, m , from 7.14 for the sound joint to 3.41 for the oxide inclusion defect, 3.19 for the tunnel defect, and 2.74 for the LOP defect (Tab. 3). Building on the fractographic, the physical origins of this variation are discussed below.

The fatigue process in metal comprises two distinct stages—crack initiation and stable crack propagation, which process fundamentally different sensitivities to the nominal stress amplitude, $\Delta\sigma$ [30,31].

The crack initiation stage involves a sequence of processes, including cyclic slip band formation, micro-crack nucleation, and coalescence, all of which are highly sensitive to $\Delta\sigma$ [30,32]. A minor reduction in the applied stress can substantially delay initiation, thereby prolonging the component's life. This high sensitivity is reflected in the S-N curve: when fatigue life

is dominated by initiation, the slope m can be significantly greater than the value of 3 typically recommended for as-welded joints. For instance, the International Institute of Welding (IIW) fatigue design recommendations now specify a flatter slope of $m = 4$ for weld toes that have been improved by grinding [33]. In contrast, the stable crack propagation stage is described by the Paris equation [34]:

$$\frac{da}{dN} = C\left(\Delta K\right)^{m_p} \tag{8}$$

Here, the stress intensity factor range ΔK is linearly related to the applied stress through $\Delta K = Y \cdot \Delta\sigma \cdot \sqrt{\pi a}$. Importantly, upon integrating the Paris equation to obtain the propagation life N_p, the exponent on $\Delta\sigma$ remains m_p, giving the proportionality $N_p \propto \left(\Delta\sigma\right)^{-m_p}$. Consequently, the sensitivity of the propagation stage to $\Delta\sigma$ is governed directly by the Paris exponent. For aluminum alloys, m_p is typically on the order of 3 [34], which is substantially lower than the sensitivity characteristic of the initiation stage.

The fractographic analysis demonstrates that the fatigue failure mechanisms of the sound joint and the three defective joints are fundamentally different. These differences dictate the degree to which the crack initiation stage is altered, which in turn is reflected in the m value.

- Sound joint: The fracture origin appears flat and featureless under SEM, with no visible fatigue striations (Fig. 7(a)). This indicates that the joint underwent a full crack initiation process. Total life is therefore dominated by this highly stress-sensitive stage, resulting in the high m value of 7.14.
- LOP defect: The sharp, L-shaped tip of this defect (Fig. 2(c)) creates a severe local stress concentration. Clear fatigue striations are observed directly at the tip (Fig. 18(a)), confirming that the initiation stage has been largely bypassed. The vary low m value of 2.74, which approaches the Paris exponent m_p, further corroborates that total life is primarily consumed by stable crack propagation.
- Oxide inclusion and tunnel defects: These two defects represent intermediated cases. Fractographic observations show that cracks initiated at the oxide-matrix interface (Fig. 11(a)) and at the junction between the tunnel and kiss bond defects (Fig. 15(a)), respectively. In both cases, a certain amount of cyclic plastic accumulation was still required before a dominant crack could form. Their intermediate m values (3.41 and 3.39) indicate that total fatigue life is governed by a combination of both the initiation and propagation stages.

In summary, the geometric sharpness and interfacial bonding state of a defect govern the extent to which the crack initiation stage is altered. This, in turn, determines whether the dominant failure mode shifts from initiation to stable propagation. Because the two stages have intrinsically different sensitivities to $\Delta\sigma$, this shift is manifested as a systematic variation in the S-N curve slope, m. This physical link explains why the LOP defect is the most detrimental: its severe geometric discontinuity and metallurgical non-bonding serve as a form of' pre-existing damage', most effectively shifting the failure mode towards propagation control. The proposed association connects a macroscopic performance parameter (m) with the underlying microscopic fracture mechanism, providing a physical basis for the fatigue assessment of FSW joints containing defects.

It should be noted that the discussion regarding the proportion of life spent in the initiation versus propagation stages is a qualitative inference derived from fractographic evidence and mechanical property data. A precise quantitative characterization still requires future work integrating crack growth rate measurements with detailed fracture mechanics analysis.

CONCLUSIONS

(1) Through orthogonal experimental optimization, the optimal FSW parameters for 2 mm -thick AA2024-T3 aluminum alloy sheets were identified: a welding speed of 200 mm/min and a rotational speed of 1000rpm. The sound joint achieved a tensile strength of 431 MPa, corresponding to 92.7% of the base material strength. On this basis, three types of typical defective joints –containing oxide inclusions, tunnel defects, and LOP defects—were fabricated by deliberately adjusting the welding conditions. The characteristic sizes of these defects were kept within the range of 0.2 mm-0.5 mm.

(2) The three types of defects substantially impaired the fatigue performance of the joints. Under constant amplitude loading at a stress ratio of $R = 0.1$ and a target life of 2×10^6 cycles, the fatigue strength retention percentages, defined as the ratio of the fatigue strength of each defective joint to that of the sound joint (152.7 MPa), were 34.8%, 28.2%, and 13.4% for the joints with oxide inclusions, tunnel defects, and LOP defects, respectively. The corresponding severity ranking is therefore LOP defect > tunnel defect > oxide inclusion defect.
(3) The fatigue fracture location and the underlying micro-mechanisms differed with defect type. The sound joint fractured either in the base material or near the shoulder edge on the advancing side, with the initiation site being flat and devoid of fatigue striations. In the case of oxide inclusions, debonding at the matrix-oxide interface created local stress concentrations. The tunnel defect, coupled with kiss-bond features, led to multiple crack initiation sites. The lop defect appeared as an L-shaped unbonded gap, the tip of which directly served as the fatigue crack initiation site. As a core, the failure of all three defective joints lies in the disruption of microstructural continuity and the degradation of local metallurgical bonding quality.
(4) The defects caused a systematic decrease in the slope m of the S-N curves. The sound joint exhibited a m-value of 7.14, significantly exceeding the typical range for fusion welds. The m-value of the joints with oxide inclusions, tunnel defects, and lop defects fell to 3.41, 3.39 and 2.74, respectively—approaching the Paris exponent m_p for aluminum alloy. This progressive decline in m reflects a shift in the dominant fatigue failure mode from 'initiation-dominated', which is highly sensitive to $\Delta\sigma$, to 'propagation-dominated', which is far less sensitive. The origin of this shift is that the geometric sharpness and interfacial bonding state of the defect, because of its severe geometric discontinuity and complete absence of metallurgical bonding, compresses the initiation stage the most and is therefore the most damaging.
(5) The high fatigue reliability of FSW joints depends critically on the microstructural soundness and interfacial metallurgical quality of the weld zone. In the welding of aircraft skin structures made of aluminum alloys, it is essential to eliminate lop defects through rigorous process control and to suppress the formation of oxide inclusions and tunnel defects as far as possible. The defect-fatigue performance correlations and the evolution of the m-parameter established in this work can provide theoretical guidance and experimental support for fatigue-resistant design, defect-tolerance assessment, and welding process optimization of FSW structures.

ACKNOWLEDGEMENT

This work was supported by the Natural Science Basic Research Plan in Shaanxi Province of China (grant number: 2025SYS-SYSZD-109); and the Autonomous Research Project of the National Key Laboratory of Strength and Structural Integrity (LSSIZZYJ202403).

DECLARATION OF INTERESTS

The authors declare that they have no known competing financial interests or personal relationships that could have appeared to influence the work reported in this paper.

REFERENCES

[1] Zorin, I.A., Pisarev, V.S., Eleonsky, S.I., Elkin, A.S., Tyurina, G.V., Statnik, E.S., Salimon, A.I. and Korsunsky, A.M. (2026). Multimodal residual stress evaluation following one-sided dimpling in a Ti-6Al-4V alloy plate, Fracture and Structural Integrity, 77, pp. 1–12. DOI: https://doi.org/10.3221/IGF-ESIS.77.01
[2] Jiang, X. and Chen, S. (2026). Friction stir welding of aluminum and steel-material flow-A review, J. Manuf. Process., 165, pp. 359–375. DOI: https://doi.org/10.1016/j.jmapro.2026.02.022
[3] Wu, C., Wang, J., Wang, Q., et al. (2024). 7075 aluminum alloy friction stir welding (FSW): Quality analysis and mechanical properties with WC-Co tool, Mater. Today Commun., 38, pp. 108203. DOI: https://doi.org/10.1016/j.mtcomm.2024.108203
[4] Yang, B.H. and Lu, X.H. (2025). Online prediction of joint mechanical properties of FSW thick AA2219-T8 based on multi-source information fusion using 1DCNN, Proc. Inst. Mech. Eng. B J. Eng. Manuf., 239, pp. 1491–1508. DOI: https://doi.org/10.1177/09544054241272748

[5] Tayebi, M., Eivani, A.R., Majidifar, A., Parsa, S.A., Mehdizade, M., Lalegani, Z. and Jafarian, H.R. (2026). A review of friction stir welding: from fundamentals to applications with a focus on brass alloys, Mater. Des., 261, pp. 115358. DOI: https://doi.org/10.1016/j.matdes.2026.115358
[6] Niu, X., He, C., Zhu, S.-P., Foti, P., Berto, F., Wang, L., Liao, D. and Wang, Q. (2024). Defect sensitivity and fatigue design: Deterministic and probabilistic aspects in additively manufactured metallic materials. Progress in Materials Science, 144, 101290. DOI: https://doi.org/10.1016/j.pmatsci.2024.101290
[7] Yang, W., Li, T., Yang, H., Zhao, Z., Sun, S., Li, L. and Yue, Z. (2025). Additively manufactured mechanical meta-materials: manufacturing defects, process-defect relationship and evaluation of mechanical properties considering defects. International Journal of Structural Integrity, 16(6), 1469–1528. DOI: https://doi.org/10.1108/IJSI-03-2025-0058
[8] Nandan, R., DebRoy, T. and Bhadeshia, H.K.D.H. (2008). Recent advances in friction-stir welding - Process, weldment structure and properties, Prog. Mater. Sci., 53, pp. 980–1023. DOI: https://doi.org/10.1016/j.pmatsci.2008.05.001
[9] Thomas, W.M., Nicholas, E.D., Needham, J.C., et al. (1991). Friction stir welding, UK Patent Application No. 9125978.8.
[10] Shi, C., Sun, H., Liu, C., et al. (2022). Effect of water cooling on microstructure and mechanical properties of friction stir welded dissimilar 2A12/6061 aluminum alloys, Mater. Res. Express, 9, pp. 056510. DOI: https://doi.org/10.1088/2053-1591/ac6d4c
[11] Majeed, T., Siddiquee, A.N. and Mehta, Y. (2022). Effect of friction stir welding parameters on microstructure-based defect formation and mechanical properties of tailor welded blanks, Mater. Today Commun., 33, pp. 104505. DOI: https://doi.org/10.1016/j.mtcomm.2022.104505
[12] Dickerson, T.L. and Przydatek, J. (2003). Fatigue of friction stir welds in aluminium alloys that contain root flaws, Int. J. Fatigue, 25, pp. 1399–1409. DOI: https://doi.org/10.1016/S0142-1123(03)00060-4
[13] Zhou, C., Yang, X. and Luan, G. (2006). Effect of root flaws on the fatigue property of friction stir welds in 2024-T3 aluminum alloys, Mater. Sci. Eng. A, 418, pp. 155–160. DOI: https://doi.org/10.1016/j.msea.2005.11.042
[14] Papadopoulos, M. and Pantelakis, S. (2017). Fatigue testing of 2198 T8 FSW aluminum alloy with and without LoP defect, Int. J. Struct. Integr., 8, pp. 496–504. DOI: https://doi.org/10.1108/IJSI-01-2017-0003
[15] Rek, R. and Kadlec, M. (2014). Friction stir welded structures: Kissing bond defects, Int. J. Tetraspace Sci. Eng., 6, pp. 77–83.
[16] Sonsino, C.M. (2007). Fatigue testing under variable amplitude loading, Int. J. Fatigue, 29, pp. 1080–1089. DOI: https://doi.org/10.1016/j.ijfatigue.2006.10.011
[17] Song, X., Zhu, S.-P., He, J.-C., Gao, J.-W., Liu, Q., Qin, S. and Wang, Q. (2026). Generalized damage tolerance framework for crack growth and failure assessment. International Journal of Mechanical Sciences, 319, 111565. DOI: https://doi.org/10.1016/j.ijmecsci.2026.111565
[18] Sutton, M.A., Yang, B., Reynolds, A.P., et al. (2002). Microstructural studies of friction stir welds in 2024-T3 aluminum, Mater. Sci. Eng. A, 323, pp. 160–166. DOI: https://doi.org/10.1016/S0921-5093(01)01358-2
[19] Jata, K.V., Sankaran, K.K. and Ruschau, J.J. (2000). Friction-stir welding effects on microstructure and fatigue of aluminum alloy 7050-T7451, Metall. Mater. Trans. A, 31, pp. 2181–2192. DOI: https://doi.org/10.1007/s11661-000-0141-5
[20] Pujono, Ilman, M.N., Muslih, M.R., et al. (2024). Minimizing residual stress and fatigue crack propagation rate of FSW joints of AA2024-T3 by transient thermal tensioning: Effect of heater distance, Int. J. Lightweight Mater. Manuf., 7, pp. 668–677. DOI: https://doi.org/10.1016/j.ijlmm.2024.03.006
[21] Das, D., Bag, S., Pal, S., et al. (2024). A review on phenomenological model subtleties for defect assessment in friction stir welding, J. Manuf. Process., 120, pp. 641–679. DOI: https://doi.org/10.1016/j.jmapro.2024.04.063
[22] Peel, M., Steuwer, A., Preuss, M., et al. (2003). Microstructure, mechanical properties and residual stresses as a function of welding speed in aluminium AA5083 friction stir welds, Acta Mater., 51, pp. 4791–4801. DOI: https://doi.org/10.1016/S1359-6454(03)00319-7
[23] Liu, P., Feng, K., Xu, S., et al. (2017). Study on precipitated phases dislocations and hardness in the HAZ of friction stir welded joint of 2024 aluminum alloy, Kovove Mater., 55, pp. 357–361. DOI: https://doi.org/10.4149/km_2017_5_357
[24] Malopheyev, S., Vysotskiy, I., Zhemchuzhnikova, D., et al. (2020). On the fatigue performance of friction stir welded aluminum alloys, Materials, 13, pp. 4246. DOI: https://doi.org/10.3390/ma13194246
[25] McDowell, D.L., Gall, K., Horstemeyer, M.F., et al. (2003). Microstructural-based fatigue modeling of cast A356-T6 alloy, Eng. Fract. Mech., 70, pp. 49–80. DOI: https://doi.org/10.1016/S0013-7944(02)00021-8

[26] Lei, Z., Junji, S., Atsushi, F., et al. (2014). Role of eutectic silicon particle in fatigue crack initiation and propagation and fatigue strength characteristics of cast aluminum alloy A356, Eng. Fract. Mech., 115, pp. 1–12. DOI: https://doi.org/10.1016/j.engfracmech.2013.10.018
[27] Lomolino, S., Tovo, R. and dos Santos, J. (2005). On the fatigue behaviour and design curves of friction stir butt-welded Al alloys, Int. J. Fatigue, 27, pp. 305–316. DOI: https://doi.org/10.1016/j.ijfatigue.2004.06.013
[28] Shahani, A.R. and Shakeri, I. (2020). Experimental evaluation of fatigue behaviour of thin Al5456 welded joints, Fatigue & Fracture of Engineering Materials & Structures, 43(5), pp. 965–977. DOI: https://doi.org/10.1111/ffe.13173.
[29] Hobbacher, A.F. and Baumgartner, J. (2024). Recommendations for Fatigue Design of Welded Joints and Components, 3rd ed., IIW Collection. Cham: Springer. DOI: https://doi.org/10.1007/978-3-031-57667-6.
[30] Suresh, S. (1998). Fatigue of Materials, 2nd ed. Cambridge: Cambridge University Press. ISBN: 9780521578479.
[31] Schijve, J. (2009). Fatigue of Structures and Materials, 2nd ed. Dordrecht: Springer. DOI: https://doi.org/10.1007/978-1-4020-6808-9.
[32] Forsyth, P.J.E. (1963). Fatigue damage and crack growth in aluminium alloys. Acta Metallurgica, 11(7), pp. 703–715. DOI: https://doi.org/10.1016/0001-6160(63)90008-7.
[33] Baumgartner, J., Hobbacher, A.F. and Lefebvre, F. (2024). Recent update of the IIW-recommendations for fatigue assessment of welded joints and components, Procedia Structural Integrity, 57, pp. 618–624. DOI: https://doi.org/10.1016/j.prostr.2024.03.068.
[34] Paris, P. and Erdogan, F. (1963). A critical analysis of crack propagation laws. Journal of Basic Engineering, 85(4), pp. 528–534. DOI: https://doi.org/10.1115/1.3656900.